A combined fit of total scattering and extended X-ray absorption fine structure data for local-structure determination in crystalline materials
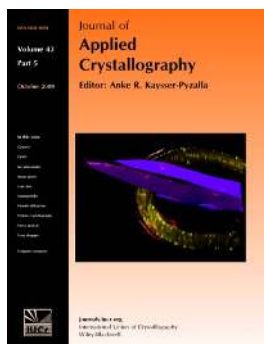
V. Krayzman, I. Levin, J. C. Woicik, Th. Proffen, T. A. Vanderah and M. G. Tucker

Many research topics in condensed matter research, materials science and the life sciences make use of crystallographic methods to study crystalline and non-crystalline matter with neutrons, X-rays and electrons. Articles published in the *Journal of Applied Crystallography* focus on these methods and their use in identifying structural and diffusion-controlled phase transformations, structure–property relationships, structural changes of defects, interfaces and surfaces, *etc.* Developments of instrumentation and crystallographic apparatus, theory and interpretation, numerical analysis and other related subjects are also covered. The journal is the primary place where crystallographic computer program information is published.

Crystallography Journals Online is available from journals.iucr.org

A combined fit of total scattering and extended X-ray absorption fine structure data for local-structure determination in crystalline materials

V. Krayzman,[a,b] I. Levin,[a]* J. C. Woicik,[a] Th. Proffen,[c] T. A. Vanderah[a] and M. G. Tucker[d]

[a]Ceramics Division, National Institute of Standards and Technology, Gaithersburg, MD 20899, USA, [b]Department of Materials Science and Engineering, University of Maryland, College Park, MD 20742, USA, [c]Lujan Neutron Center, Los Alamos National Laboratory, Los Alamos, NM, USA, and [d]ISIS, Rutherford Appleton Laboratory, Didcot, UK. Correspondence e-mail: igor.levin@nist.gov

Reverse Monte Carlo (RMC) refinements of local structure using a simultaneous fit of X-ray/neutron total scattering and extended X-ray absorption fine structure (EXAFS) data were developed to incorporate an explicit treatment of both single- and multiple-scattering contributions to EXAFS. The refinement algorithm, implemented as an extension to the public domain computer software *RMCProfile*, enables accurate modeling of EXAFS over distances encompassing several coordination shells around the absorbing species. The approach was first tested on Ni, which exhibits extensive multiple scattering in EXAFS, and then applied to perovskite-like $SrAl_{1/2}Nb_{1/2}O_3$. This compound crystallizes with a cubic double-perovskite structure but presents a challenge for local-structure determination using a total pair-distribution function (PDF) alone because of overlapping peaks of the constituent partial PDFs (*e.g.* Al—O and Nb—O or Sr—O and O—O). The results obtained here suggest that the combined use of the total scattering and EXAFS data provides sufficient constraints for RMC refinements to recover fine details of local structure in complex perovskites. Among other results, it was found that the probability density distribution for Sr in $SrAl_{1/2}Nb_{1/2}O_3$ adopts T_d point-group symmetry for the Sr sites, determined by the ordered arrangement of Al and Nb, as opposed to a spherical distribution commonly assumed in traditional Rietveld refinements.

1. Introduction

Local atomic arrangements in complex crystalline materials often deviate from the average configurations described by the space-group symmetry. Common examples include solid solutions that are locally heterogeneous and systems with displacive disorder. In many cases, subtle local-structure details critically affect the functional properties of materials. Several experimental techniques can probe various aspects of local structure, but comprehensive quantitative determination of local atomic order remains a challenge (Billinge & Levin, 2007).

Extended X-ray absorption fine structure (EXAFS) has been for decades the primary tool for quantitative local-structure determination. A Fourier transform of EXAFS data yields a version of the instantaneous pair-distribution function (PDF) around the absorbing species which is modified by several nonstructural parameters that describe scattering of a photoelectron on neighboring atoms. Additionally, multiple-scattering contributions to EXAFS render it sensitive to bond angles, thereby providing three-dimensional structural infor-

mation. However, a typical distance range ($\sim$5 Å) probed by EXAFS encompasses only the first few coordination shells around the absorber, which is insufficient for analyses of nanoscale structural heterogeneities.

Another technique that emerged recently as a powerful probe of local/nanoscale atomic order relies on X-ray/neutron elastic total scattering (*i.e.* a sum of the Bragg and diffuse diffracted intensities) to extract the instantaneous atomic PDF (Egami & Billinge, 2003). This PDF is obtained *via* a Fourier transform of the properly normalized total scattering intensity. The total scattering PDF is chemically unresolved but extends over distances up to several tens of nanometres. Thus, EXAFS and X-ray/neutron total scattering provide highly complementary information. Unfortunately, quantitative refinements of local structure using a simultaneous fit of both types of data are rare (Binsted *et al.*, 2001; Winterer *et al.*, 2002; Krayzman *et al.*, 2008), in part because of the lack of appropriate software and established methodology for combined refinements.

Traditional EXAFS refinements are performed by fitting a signal, calculated for a small atomic cluster around the absorber species, to the experimental data. Nonstructural

parameters that affect EXAFS are calculated prior to refinements using *ab initio* theory (Ankudinov *et al.*, 1998). Local structure is described using a small number of independent variables that include coordination numbers, interatomic distances and their associated Debye–Waller (D–W) factors, and, if multiple scattering is included, bond angles (Ravel & Newville, 2005). A PDF underlying the EXAFS signal is commonly assumed to be a sum of the Gaussian peaks. Non-Gaussian distance distributions can be modeled using higher-order cumulants, but reliable determination of these parameters from EXAFS alone is rarely feasible.

The total scattering PDF can yield model-independent local-structure information by fitting Gaussian profiles to the first few PDF peaks (Bozin *et al.*, 2007; Qiu *et al.*, 2005); however, the applicability of these analyses is limited by the peak overlap. Typically, a structural model is assumed and refined against the experimental data. One approach to PDF analyses relies on a small unit cell, frequently under symmetry constraints, to describe the structure (Farrow *et al.*, 2007). Information on local, medium-range and long-range atomic order can be deduced by selecting an appropriate distance range for a PDF fit: that is, the structural model and interpretation of the refined parameters may vary with the distance range used. These Rietveld-style real-space refinements are gaining popularity because of the small number of structural variables, which facilitates interpretation of the results. However, despite evident strengths and notable successes, especially as applied to nanomaterials (Masadeh *et al.*, 2007; Pradhan *et al.*, 2007), this method suffers from several limitations. For example, it cannot provide accurate treatments of solid solutions, non-Gaussian distributions of interatomic distances and local chemical/displacement correlations.

In contrast, reverse Monte Carlo (RMC) refinements that employ large atomic ensembles to fit experimental data using a variation of the Metropolis algorithm enable explicit treatment of atomic disorder without *a priori* assumptions about the distribution of interatomic distances (McGreevy, 2001). For most systems, the PDF alone is insufficient to recover a complete set of essential structural characteristics. Simultaneous fitting of the total scattering data in real and reciprocal spaces partly alleviates this problem, while additional inclusion of Bragg intensities as a separate data set further constrains average-structure characteristics (Tucker *et al.*, 2007). However, in many cases, even these measures cannot prevent unphysical distances/configurations and, therefore, various geometric restraints must be imposed on interatomic distances and bond angles in order to obtain chemically sound structural models (Tucker *et al.*, 2007). The situation is particularly difficult for structures that exhibit a substantial overlap of the peaks of the constituent partial PDFs.

Recently, we demonstrated that simultaneous fitting of X-ray/neutron total scattering and EXAFS data diminishes and sometimes completely obviates the need for geometric restraints (Krayzman *et al.*, 2008). However, these studies considered only single-scattering contributions to EXAFS, which significantly limited the extent of EXAFS data included

in the refinements. In the present work, we developed an algorithm for a joint RMC fit of the total scattering and EXAFS data that enables accurate treatment of both single- and multiple-scattering EXAFS contributions; like the previous version, this algorithm was implemented as an extension to the public domain *RMCProfile* computer code (Tucker *et al.*, 2007). The software enables accurate modeling of EXAFS data over a distance range up to $\sim$5 Å, which includes several coordination shells around the absorber.

We first tested this approach on Ni metal because it exhibits extensive multiple-scattering effects in EXAFS data. Our combined refinements reproduced the experimental data and yielded Ni—Ni displacement correlation parameters that matched those obtained from the direct analyses of peak widths in the neutron PDF. Subsequently, we applied the method to $Sr(Al_{1/2}Nb_{1/2})O_3$ and its solid solutions with $SrTiO_3$. $Sr(Al_{1/2}Nb_{1/2})O_3$ crystallizes with a relatively simple cubic double-perovskite structure but presents a challenge for local-structure refinements using either total scattering data or EXAFS alone because of the overlap of the Al—O and Nb—O peaks in the total PDF, and the inability to measure Al EXAFS owing to its overlap with an Sr L-edge.

2. Experimental

The SAN ($SrAl_{1/2}Nb_{1/2}O_3$) and SANT ($SrAl_{0.4325}Nb_{0.4325}Ti_{0.135}O_3$) samples were prepared using solid-state methods from $SrCO_3$ (99.99%), Al_2O_3 (99.99%, 0.3 µm), Nb_2O_5 (99.9985%) and TiO_2 (< 10 p.p.m. P). Prior to heating, the samples ($\sim$20 g each) were mixed by grinding with an agate mortar and pestle for 30 min, pelletized, and placed on beds of same-composition sacrificial powder supported on alumina ceramic. After an initial overnight calcination at 1223 K, the samples were heated at 1473 K (18 h), then at 1833 K (112 h) and then again at 1833 K (110 h); after this final heating the samples were cooled to 1723 K and annealed at that temperature for 144 h. Samples were furnace-cooled to 973 K and then air-quenched on the bench-top. X-ray diffraction patterns were collected using a powder diffractometer equipped with a Ge incident beam monochromator (Cu $K\alpha_1$ radiation) and a position-sensitive detector. Both the SAN and the SANT samples contained just-detectable (< 1%) amounts of $Sr_5Nb_4O_{15}$ in addition to the major perovskite-like phase. The SAN sample exhibited a highly ordered arrangement of Al and Nb as confirmed by Rietveld refinements using X-ray diffraction data. The SANT composition with 13.5% Ti was selected from our studies of *B*-cation order/disorder behavior in the $SrAl_{1/2}Nb_{1/2}O_3$–$SrTiO_3$ system, to be described elsewhere. This SANT composition exhibited weak but still discernible long-range Al/Nb order, making it a suitable candidate for comparison with SAN.

Neutron total scattering data were collected at room temperature on the NPDF instrument at the Lujan Neutron Scattering Center (Los Alamos National Laboratory). The samples were loaded in vanadium containers. The *PDFGetN* software (Peterson *et al.*, 2000) was used for data correction and normalization. The PDF, $G(r)$, was obtained as a sine

Fourier transform of the normalized scattering intensity $S(Q)$ according to

$$G(r) = (2/\pi) \int_0^{Q_{max}} Q[S(Q) - 1] \sin(Qr) \, dQ. \qquad (1)$$

A value of $Q_{max} \simeq 35$ Å was used in the Fourier transform. EXAFS data for the K-edges of Ni, Nb and Sr were measured at the NIST X23A2 beamline of the National Synchrotron Light Source. The data were collected in transmission using a metal foil for Ni and powder samples for SAN/SANT. The *Athena* software package (Ravel & Newville, 2005) was used to extract the EXAFS oscillations. Preliminary EXAFS fitting was accomplished with the *Artemis* software (Ravel & Newville, 2005).

Conventional Rietveld refinements to determine the average structures were conducted using the *GSAS* software package and the neutron diffraction data. The refined lattice parameters and atomic positional parameters were used to generate starting atomic configurations for the RMC refinements. These refinements were performed using the *RMCProfile* software (Tucker *et al.*, 2007), which was modified to enable a simultaneous fit of the total scattering and EXAFS data. *RMCProfile* adopts the PDF representation $T(r)$, which is related to $G(r)$ as

$$T(r) = \left(\sum_{i=1}^{n} c_i b_i \right)^2 [G(r) + 4\pi r \rho_0], \qquad (2)$$

where ρ_0 is the average atom number density, c_i is the fraction of atoms of type i and b_i is the corresponding neutron scattering length.

3. EXAFS fit in combined RMC refinements

The RMC method relies on a Monte Carlo 'random walk' algorithm to identify a configuration that yields the best match to experimental data. Unlike downhill algorithms used in Rietveld-style refinements, atomic moves that worsen the discrepancy between the calculated and experimental data are accepted with a probability that decays exponentially as the misfit increases. The target function, R_{tot}^2, minimized during the fit, is the total residual

$$R_{tot}^2 = \sum_i R_i^2 = \sum_i (1/\sigma_i^2) \sum_j \left(Y_j^{calc} - Y_j^{exp} \right)^2, \qquad (3)$$

where R_i is the agreement factor for the ith data set (or restraint), Y_j^{calc} and Y_j^{exp} refer to the calculated and experimental signals/restraints, respectively, j specifies individual data points in each data set, and $1/\sigma_i^2$ is the weight that controls the contribution of the ith data set to the target function. Calculations of the target function components associated with the PDF, $S(Q)$, Bragg intensities and various polyhedral constraints have been described previously (Tucker *et al.*, 2007). Therefore, we limit the discussion here to the details specific to EXAFS.

In the present RMC refinements, the contributions of instantaneous local atomic configurations to the EXAFS signal are included explicitly without any assumptions about the type of atomic distributions or atomic motions. The single-scattering contribution to EXAFS for the absorbing atom i can be calculated as (Mustre de Leon *et al.*, 1991)

$$\chi_i^{(single)}(k) = \sum_j \frac{S_{0i}^2 \Re_i(k) |F_j(\pi, k)|}{k r_{ij}}$$
$$\times \sin[2k r_{ij} + \psi_i(k) + \varphi_j(\pi, k)] \exp[-2r_{ij}/\lambda(k)], \qquad (4)$$

where S_{0i}^2 is the amplitude reduction factor, $\Re_i(k)$ is the total central atom loss factor, j specifies the neighboring atoms around the absorber, r_{ij} is the interatomic separation, k is the photoelectron wavenumber, $F_j(\pi, k) = |F_j(\pi, k)| \exp[\varphi_j(\pi, k)]$ is the complex backscattering amplitude, $\psi_i(k)$ is the total scattering phase shift for the absorbing atom and $\lambda(k)$ is the photoelectron mean free path. The summation is carried out over all the neighboring atoms within a sphere of radius R_{max}, and the resulting EXAFS signal is averaged over all the absorber atoms in the configuration. Common multiple-scattering processes that contribute significantly to EXAFS include double and triple scattering (Appendix A). Double-scattering contributions can be calculated according to

$$\chi_i^{(double)}(k) = \sum_{j,n} \frac{S_{0i}^2 \Re_i(k) |F_{jn}^{eff(2)}(\vartheta, k)|}{k r_{ij} r_{jn} r_{ni}}$$
$$\times \sin[2k r_{eff} + \psi_i(k) + \varphi_{jn}^{eff(2)}(\vartheta, k)] \exp[-2r_{eff}/\lambda(k)], \qquad (5)$$

where $F_{jn}^{eff(2)}(\vartheta, k)$ is the effective amplitude for the scattering angle ϑ (see Appendix A for details) and $r_{eff} = (r_{ij} + r_{jn} + r_{ni})/2$. Triple-scattering contributions are described using analogous equations.

The only structural parameter that enters equation (4) for single scattering is the interatomic distance r_{ij}: that is, the single-scattering EXAFS is uniquely determined by the absorber–scatterer partial PDF. For multiple scattering, EXAFS depends on three-body distribution functions that can be readily computed for any given atomic configuration.

According to our computational procedure, all nonstructural parameters (*i.e.* scattering amplitudes, phase shifts *etc.*) are calculated prior to refinements using the average-structure model. Variations of scattering amplitudes due to small changes in interatomic distances during refinements can be neglected, as commonly assumed in traditional EXAFS analyses (Ravel & Newville, 2005). Values of $F_{jn}^{eff(2)}(\vartheta, k)$ and $F_{jn}^{eff(3)}(\vartheta, k)$ for double and triple scattering, respectively, are calculated on a fixed ϑ grid and then linearly interpolated for an arbitrary angle during the RMC fit. EXAFS data can be fitted in either k or r space; however, an r-space fit is typically preferred. In the first step of the refinements, the EXAFS signal $\chi(k)$ is calculated for all the absorber atoms in the starting atomic configuration according to equations (3) and (4) and then Fourier transformed into real space as

$$\tilde{\chi}^{(n)}(r) = [1/(2\pi)^{1/2}] \int_{k_1}^{k_2} \exp(2ikr) k^n \chi(k) \, dk, \qquad (6)$$

where n is the k-weighting factor. After each atomic move, EXAFS contributions for all the absorber atoms within a

Table 1
Displacement correlation parameters for successive nearest neighbors (NN) in Ni calculated for the RMC-refined configuration.

NN	1st $\langle 011 \rangle$	2nd $\langle 002 \rangle$	3rd $\langle 012 \rangle$	4rd $\langle 022 \rangle$	5rd $\langle 013 \rangle$
Longitudinal	0.36	0.02	0.08	0.16	0.02
Transverse	0.09	0.04	–	–	–

sphere of radius R_{max} are recalculated. Typically, R_{max} is limited to ≤ 5 Å to maintain reasonable computing times.

Traditional EXAFS analyses often treat an amplitude reduction factor (S_0^2) and a threshold energy (E_0) as adjustable parameters. Refinements of S_0^2 compensate for systematic errors due to sample/instrument problems (*i.e.* sample inhomogeneity), whereas adjustments of E_0 correct deficiencies in the muffin tin interatomic potentials and scattering amplitudes. Moreover, separate E_0 shifts (ΔE_0) often must be introduced for distinct absorber–scatterer paths. In our RMC refinements, both S_0^2 and E_0 were kept fixed. Values of these parameters are determined using traditional EXAFS fits prior to the RMC refinements. According to our results, self-consistent potential calculations implemented in version 8.20 of *FEFF* (Ankudinov *et al.*, 2002) are sufficiently accurate to obviate the need for multiple values of ΔE_0.

Several EXAFS data sets can be included in the refinements. For a real-space fit, the contribution of each data set to the total residual is calculated as

$$R_{EXAFS}^2 = \frac{1}{\sigma_{EXAFS}^2} \left\{ \sum_i \left| \mathrm{Re}\left[\tilde{\chi}_{calc}^{(n)}(r_i) - \tilde{\chi}_{exp}^{(n)}(r_i) \right] \right|^2 \right. $$
$$\left. + \sum_i \left| \mathrm{Im}\left[\tilde{\chi}_{calc}^{(n)}(r_i) - \tilde{\chi}_{exp}^{(n)}(r_i) \right] \right|^2 \right\}, \quad (7)$$

where $1/\sigma_{EXAFS}^2$ is the weight assigned to a particular EXAFS data set and the subscripts calc and exp refer to calculated and experimental values, respectively.

In most cases, both total scattering and EXAFS are dominated by systematic errors and, therefore, a rigorous assignment of weights in the total agreement function [equation (3)] is unfeasible. We implemented a weighting scheme that adjusts values of σ_i^2 [equation (3)] during the refinements to maintain the relative contributions of different data sets [*i.e.* R_i^2 in equation (3)] to the total-agreement function fixed. The reliability of the refined structural characteristics was analyzed by repeating the analyses using different distributions of the weights.

4. Results and discussion

4.1. Nickel metal

Metallic nickel was chosen as a test system because a Fourier transform of the Ni *K*-edge EXAFS data features a well separated first-nearest-neighbor peak and strong multiple-scattering effects within the collinear chains formed by the first and fourth nearest neighbors. This type of EXAFS data is typical for all face centered cubic metals.

Rietveld refinements using neutron diffraction data yielded an Ni atomic displacement parameter (ADP) $U_{iso} = 0.00573$ (3) Å^2. The first-nearest-neighbor peak in the neutron PDF was satisfactorily fitted using a Gaussian profile with $r_{Ni-Ni} = 2.487$ (1)[1] and $\sigma_{Ni-Ni}^2 = 0.0064$ (1) Å^2. A single-shell fit of the first peak in EXAFS generated $r_{Ni-Ni} = 2.485$ (2) Å and $\sigma_{Ni-Ni}^2 = 0.0064$ (2) Å^2, which agree with the PDF-derived values. Refinement of S_0^2 and ΔE_0 during the EXAFS fit produced $S_0^2 = 0.84$ (2) and $\Delta E_0 = +3.3$ eV (hereafter, ΔE_0 is specified with respect to the edge inflection point). The refined value of S_0^2 was smaller than $S_0^2 = 0.953$ predicted by *FEFF8.20*; however, such relatively small differences are not unusual as a result of experimental errors. Refinements using a fixed value of $S_0^2 = 0.953$ yielded $\sigma^2 = 0.0073$ (2) Å^2. Good agreement between the r_{Ni-Ni} and σ^2 values obtained by fitting the first-nearest-neighbor peaks in the PDF and EXAFS suggests that the two data sets are consistent with each other and, therefore, amenable to simultaneous refinements.

RMC refinements were performed using an atomic configuration of 4000 atoms arranged in the cubic $10a \times 10a \times 10a$ box ($a = 3.5323$ Å is the lattice parameter of Ni). The total PDF, EXAFS data and Bragg profile were fitted simultaneously. The fitting ranges were 2.1–17.5 Å for the PDF and 1.5–5.2 Å for EXAFS. The profile shape and background parameters for the Bragg profile were obtained using Rietveld refinements and kept fixed during the RMC fit. Satisfactory agreement between the calculated and experimental profiles for all the data sets was obtained (Fig. 1).

The D–W factor $\sigma_{Ni-Ni}^2 \simeq 0.0064$ Å^2 for the first Ni—Ni coordination in both the PDF and EXAFS, as estimated from the first peak fit, is significantly smaller than the value of $2U_{iso} \simeq 0.0114$ Å^2 expected for uncorrelated atomic motion. The correlation parameter $\phi = 1 - \sigma_{Ni-Ni}^2/(2U_{iso})$ is equal to 0.4 (1), which corresponds to a preference for the in-phase displacements of the nearest-neighbor Ni atoms.

RMC refinements enable calculations of any type of interatomic correlations. For example, displacement pair correlations can be evaluated as

$$\phi(\mathbf{n}_1, \mathbf{n}_2) = \frac{\langle (\mathbf{u}_i \cdot \mathbf{n}_1)(\mathbf{u}_j \cdot \mathbf{n}_2) \rangle}{\left[\langle (\mathbf{u}_i \mathbf{n}_1)^2 \rangle \langle (\mathbf{u}_j \mathbf{n}_2)^2 \rangle \right]^{1/2}}, \quad (8)$$

where $\mathbf{u}_i$ is the displacement of an atom from the lattice site i having a radius vector $\mathbf{r}_i$, $\mathbf{n}_1$ and $\mathbf{n}_2$ are the unit vectors along the directions of interest, and angular brackets indicate an average over the atomic sites i and j.

Table 1 summarizes displacement correlation parameters calculated for several successive coordination shells using the refined RMC configuration. Both longitudinal and transverse correlations were considered. The correlation parameters calculated from our RMC-refined configuration up to the fourth coordination shell agree reasonably well with those obtained from the peak widths in the neutron PDF. Our values for the correlation parameters also agree with those reported previously by Jeong *et al.* (2003).

---

[1] Hereafter, the numbers in parentheses refer to a single estimated standard deviation.

4.2. Double Perovskites SrAl$_{0.5}$Nb$_{0.5}$O$_3$ and SrAl$_{0.4325}$-Nb$_{0.4325}$Ti$_{0.135}$O$_3$

4.2.1. Rietveld and traditional EXAFS refinements. SrAl$_{1/2}$-Nb$_{1/2}$O$_3$ (SAN) crystallizes with a cubic perovskite-like structure that features rocksalt-type 1:1 order of Al and Nb on the octahedral B sites (Goodenough & Longo, 1970; Guo *et al.*, 1995) (Figs. 2 and 3). This ordering generates $Fm3m$ symmetry and lattice parameter $a = 7.78365\,(1)$ Å. Rietveld refinements of the SAN structure using neutron diffraction data indicate that O atoms are displaced by 0.0246 (6) Å from their ideal positions toward the smaller Al atoms so that the resulting average Al—O and Nb—O distances are 1.9213 (6) and 1.9705 (6) Å, respectively. The refined long-range order (LRO) parameter that describes a fraction Al/(Al + Nb) on the Al-rich sites was close to 1. The ADP value for Nb [$U = 0.0059\,(1)$ Å^2] is larger than that for Al [$U = 0.0042\,(2)$ Å^2].

The SrAl$_{0.4325}$Nb$_{0.4325}$Ti$_{0.135}$O$_3$ (SANT) sample crystallizes with a similar cubic $Fm3m$ structure [$a = 7.80008\,(1)$ Å] and retains a certain degree of the B-site LRO (Fig. 3). According

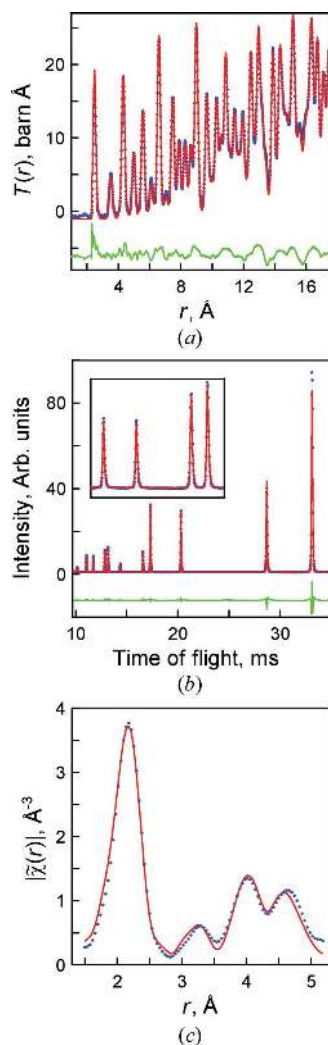to Rietveld refinements, the LRO parameter in this sample is close to 0.60. Both the charge and the ionic radius of Ti^{4+} ($R = 0.605$ Å) are between those for Al^{3+} ($R = 0.53$ Å) and Nb^{5+} ($R = 0.64$ Å) (Shannon, 1976). Therefore, we assumed a random distribution of Ti so that the compositions of the Al- and Nb-rich sublattices are [Al$_{0.2595}$Nb$_{0.173}$Ti$_{0.065}$] and [Al$_{0.173}$Nb$_{0.2595}$Ti$_{0.065}$], respectively. The short-range order (SRO) parameter that describes the probability of finding Nb in the first B-cation coordination shell around Al was esti-
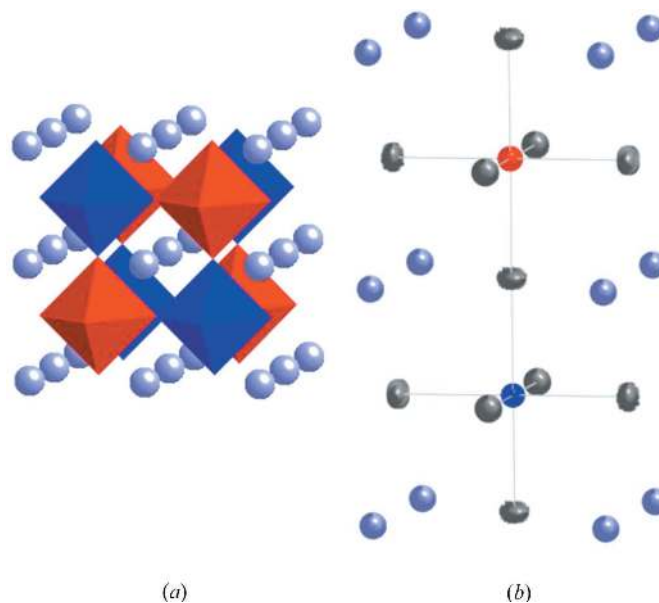

Figure 1
Experimental (doted lines) and calculated (solid lines) (*a*) $T(r)$, (*b*) Bragg and (*c*) EXAFS profiles for Ni as obtained by a simultaneous RMC fit. The inset in (*b*) displays a magnified view of the high-Q region of the Bragg profile.

Figure 2
(*a*) Schematic drawing of the SrAl$_{1/2}$Nb$_{1/2}$O$_3$ structure. [AlO$_6$] and [NbO$_6$] octahedra are indicated using different colors. (*b*) Atomic displacement parameters (70% probability) as obtained from Rietveld neutron refinements. A strong anisotropy of oxygen displacements is observed with their displacement ellipsoids flattened along the directions of the B—O bonds.
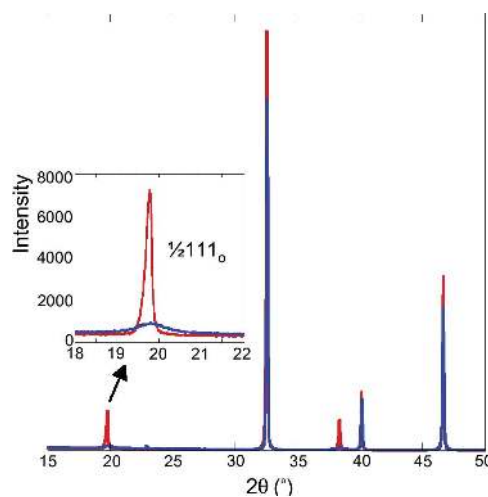

Figure 3
X-ray diffraction patterns for SAN (red) and SANT (blue). The inset displays the superlattice reflection $\frac{1}{2}111_o$, which is associated with 1:1 B-cation order (subscript 'o' refers to an ideal ∼4 Å cubic perovskite cell). The ordering in SANT is significantly weaker and the ordered domains are smaller than those of SAN.

V. Krayzman *et al.* · Combining total scattering and EXAFS data

mated as 0.80 by fitting the Nb EXAFS in *Artemis*. As expected, O-atom displacements toward the Al-rich site in the partially ordered SANT structure are much smaller than those in the end compound, resulting in Al′−O and Nb′−O bond distances of 1.965 (2) and 1.978 (2) Å, respectively (Al′ and Nb′ designate the Al- and Nb-rich crystallographic sites in the average structure).

The first peak in the total PDF for SAN, which represents the sum of the Nb−O and Al−O bond-length distributions (weighted by the appropriate neutron scattering lengths), can be fitted using a narrow symmetric Gaussian function with $r_0 = 1.961$ (1) Å and $\sigma^2 = 0.0046$ (2) Å^2: that is, the Al−O and Nb−O peaks are unresolved. Likewise, the Sr−O and O−O peaks overlap completely. Thus, the PDF alone cannot provide reliable distributions of these distances.

4.2.2. RMC refinements. RMC refinements using a simultaneous fit of the total PDF, Bragg intensities, and Sr and Nb EXAFS were conducted.

Refinement details. The refinements used a configuration of 20 480 atoms arranged in a cubic box of $8a \times 8a \times 8a$ (edge length 62.27 Å) according to their expected positions in the average structure. The fitting ranges were 1.65–20.00 Å for the PDF, 1.0–4.3 Å for the Sr EXAFS and 1.0–4.2 Å for the Nb EXAFS. The EXAFS data were weighted by k^2. The RMC configuration for SAN assumed a perfect Al/Nb order.

For SANT, an explicit incorporation of the three-cation distribution on the B sites significantly increases the number of constituent partial PDFs, which complicates the analyses.

Therefore, for this sample, we introduced two effective types of B cations: Al* = $(Al_{0.865}Ti_{0.135})$ and Nb* = $(Nb_{0.865}Ti_{0.135})$. The effect of Ti substitution on the neutron total scattering was accounted for by modifying the neutron scattering lengths according to a linear mixture rule. Calculations of the modified photoelectron scattering amplitudes and phases for EXAFS are described in Appendix *B*. The initial RMC configuration for this sample was generated by starting from the ideal 1:1 order of Al* and Nb* atoms and swapping these cations until the experimental values of both the LRO and the SRO parameters were attained. The resulting cation distribution was kept fixed during the RMC fit.

In both cases, polyhedral constraints had to be applied to distances and angles within the [AlO$_6$] and [NbO$_6$] octahedra to preclude unphysical atomic configurations during the initial stages of the refinements. Previously, we showed that EXAFS is ineffective in constraining atomic moves during these initial stages, even when EXAFS data are available for both overlapped B−O peaks (Krayzman *et al.*, 2008). The weights assigned to polyhedral constraints were decreased gradually and removed completely during the final stages of the refinements. The fit was repeated three times and the structural characteristics presented below were obtained by averaging over the three resulting atomic configurations.

Scattering amplitudes and phases for modeling the Sr and Nb EXAFS were obtained using self-consistent calculations in *FEFF8.20*. Preliminary fits yielded $\Delta E_0 = -3$ eV and $\Delta E_0 = -6$ eV for Sr and Nb, respectively. Sr EXAFS, within the
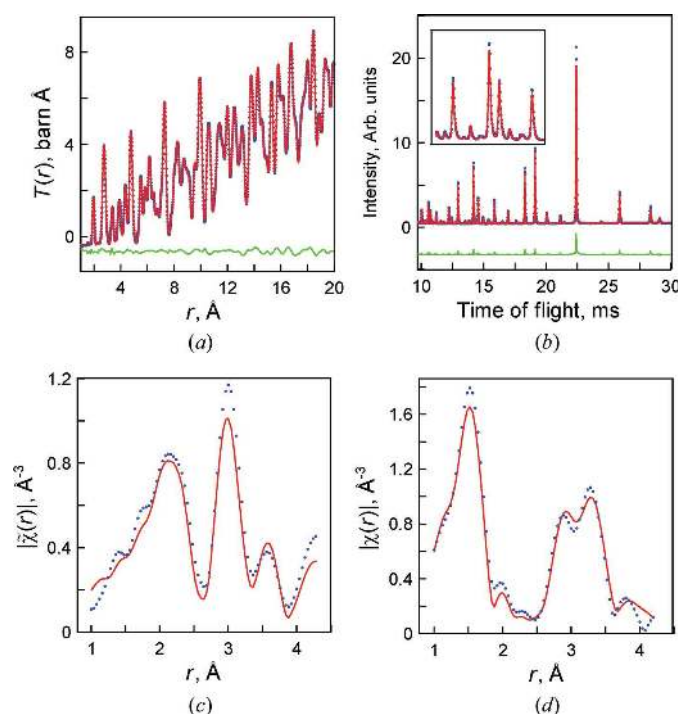

Figure 4
Experimental (dotted lines) and calculated (solid lines) (*a*) $T(r)$, (*b*) Bragg, and (*c*) Sr EXAFS and (*d*) Nb EXAFS profiles for SrAl$_{1/2}$Nb$_{1/2}$O$_3$ obtained by a simultaneous RMC fit. The inset in (*b*) displays a magnified view of the high-Q range of the Bragg profile. The k ranges used in EXAFS Fourier transforms were 3.3–13.2 Å^{-1} for Nb and 3.0–14.2 Å^{-1} for Sr.
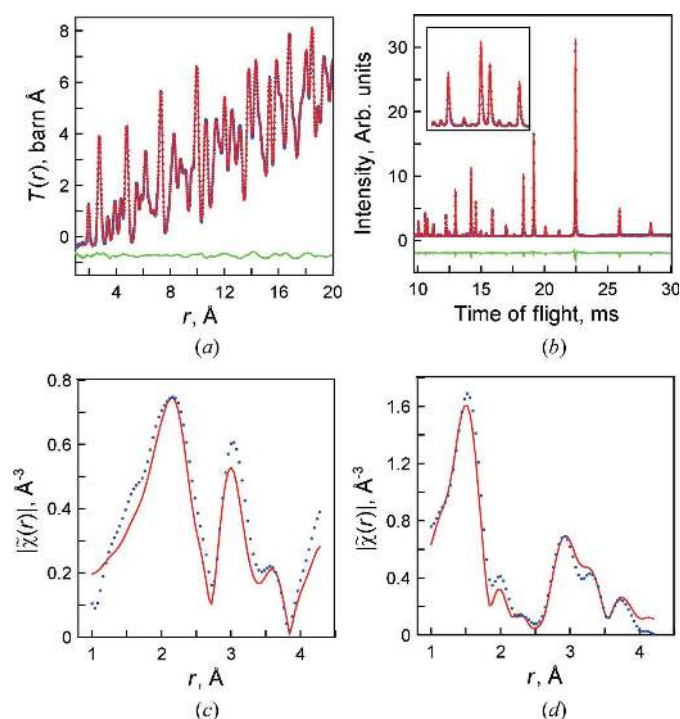

Figure 5
Experimental (dotted lines) and calculated (solid lines) (*a*) $T(r)$, (*b*) Bragg, and (*c*) Sr EXAFS and (*d*) Nb EXAFS profiles for SrAl$_{0.4325}$Nb$_{0.4325}$Ti$_{0.135}$O$_3$ obtained by a simultaneous RMC fit. The inset in (*b*) displays a magnified view of the high-Q range of the Bragg profile. The k ranges used in EXAFS Fourier transforms were similar to those for SAN (Fig. 4).

Table 2
Atomic displacement parameters (Å^2) in SAN obtained from Rietveld and RMC refinements.

ADP	Rietveld refinement	RMC fit
U_{Sr}	0.0088 (1)	0.007
U_{Al}	0.0042 (2)	0.005
U_{Nb}	0.0059 (1)	0.006
U_{O}	U_{11} = 0.0051 (1), $U_{22} = U_{33}$ = 0.0101 (1)	U_{11} = 0.006, $U_{22} = U_{33}$ = 0.011

fitting range, is dominated by single scattering. In contrast, Nb EXAFS in the range from 2.8 to 4.3 Å is strongly affected by the double- and triple-scattering events that involve B cations and O atoms; this multiple scattering contributes at distances similar to the $B-B$ separation and therefore must be taken into account. The results of the simultaneous PDF/Bragg/EXAFS fit for SAN and SANT are summarized in Figs. 4 and 5, respectively. Satisfactory agreements between the calculated and experimental profiles were obtained for all data sets.

$B-O$ distance distributions and octahedral distortions. The Nb$-$O and Al$-$O partial PDFs for SAN/SANT are shown in Fig. 6. For SAN, the first Nb$-$O peak exhibits a symmetric Gaussian shape, whereas the Al$-$O bond distance distribution is weakly asymmetric (Fig. 6a). The average instantaneous Nb$-$O (1.979 Å) and Al$-$O (1.926 Å) bond distances are larger than the distances between the corresponding average positions calculated for the same atomic configuration; the differences, albeit small, are significant and arise because of a transverse atomic motion, which is particularly pronounced for the O atoms. The ADP values calculated for the average atomic positions within the RMC-refined configuration agree well with those obtained using Rietveld refinements, including the anisotropy of the oxygen displacements and the relation $U_{\text{Nb}} > U_{\text{Al}}$ (Table 2). Table 3 compares the Nb$-$O and Sr$-$O distances and their D–W factors as determined by the combined RMC refinements with those obtained from the EXAFS data alone. The differences between the two sets of parameters are less than ± 2 s.u.; in principle, some differences are expected as a result of uncertainties in the values of S_0^2 and E_0, which correlate strongly with the D–W factors and interatomic distances, respectively. The second moment of the Nb$-$O bond distance distribution is significantly smaller than that for the Al$-$O distribution ($\sigma^2_{\text{Nb}-\text{O}} \simeq 0.003$ Å^2 < $\sigma^2_{\text{Al}-\text{O}} \simeq 0.005$ Å^2). The Nb$-$O and Al$-$O displacement correlation parameters (along the $B-O$ bonds) calculated using equation (8) are $\phi_{\text{Nb}-\text{O}}$ = 0.74 and $\phi_{\text{Al}-\text{O}} \simeq 0.50$, respectively. This difference in the Nb$-$O/Al$-$O displacement correlations can be attributed to the different strengths of the Nb$-$O (bond strength 5/6) and Al$-$O (3/6) bonds. Table 4 summarizes the correlation parameters calculated for several successive $B-O$ and $B-B$ coordination shells. The correlations weaken with increasing interatomic distances but remain significant up to the second $B-O$ and $B-B$ nearest neighbors.

For SANT, the average instantaneous distances Nb*$-$O (1.965 Å) and Al*$-$O (1.952 Å) remain distinct, but are closer in value than those for SAN (Fig. 6b); the reduced difference can be attributed to the combined effects of Ti incorporated in

Table 3
Distances and D–W factors for the Nb$-$O and Sr$-$O nearest neighbors obtained by fitting the EXAFS data in *Artemis* and by combined RMC refinements.

Coordination shell	Structural parameters	EXAFS	RMC
SrAl$_{1/2}$Nb$_{1/2}$O$_3$			
Nb$-$O	$R_{\text{Nb}-\text{O}}$ (Å)	1.984 (3)	1.979
	$\sigma^2_{\text{Nb}-\text{O}}$ (Å^2)	0.0026 (4)	0.003
Sr$-$O	$R_{\text{Sr}-\text{O}}$ (Å)	2.73 (1)	2.745
	$\sigma^2_{\text{Sr}-\text{O}}$ (Å^2)	0.011 (2)	0.013
SrAl$_{0.4325}$Nb$_{0.4325}$Ti$_{0.135}$O$_3$			
Nb$-$O	$R_{\text{Nb}-\text{O}}$ (Å)	1.97 (1)	1.965†
	$\sigma^2_{\text{Nb}-\text{O}}$ (Å^2)	0.004 (1)	0.004†
Sr$-$O	$R_{\text{Sr}-\text{O}}$ (Å)	2.72 (1)	2.764†
	$\sigma^2_{\text{Sr}-\text{O}}$ (Å^2)	0.014 (1)	0.016

† According to our model for SrAl$_{0.4325}$Nb$_{0.4325}$Ti$_{0.135}$O$_3$, RMC returns characteristics of the effective Nb*$-$O coordination as opposed to the Nb$-$O coordination probed by EXAFS (Nb* = Nb$_{0.865}$Ti$_{0.135}$).

Table 4
Longitudinal displacement correlation parameters for successive $B-O$ and $B-B$ coordination shells along the $-$Nb$-$O$-$Al$-$Nb$-$O$-$Al$-$ chains in Sr(Al$_{1/2}$Nb$_{1/2}$)O$_3$.

$B-O$			$B-B$	
Shell ⟨100⟩	$\phi_{\text{Nb}-\text{O}}$	$\phi_{\text{Al}-\text{O}}$	Shell ⟨100⟩	ϕ_{B-B}
1st	0.74	0.47	1st (Nb$-$Al)	0.33
2nd	0.160	0.26	2nd (Nb$-$Nb)	0.13
3rd	0.09	0.04	2nd (Al$-$Al)	0.13
4th	$-$0.09	0.00	3rd (Nb$-$Al)	0
5th	$-$0.08	$-$0.06		

the Nb* = (Nb$_{0.865}$Ti$_{0.135}$) and Al* = (Al$_{0.865}$Ti$_{0.135}$) atomic types, in addition to substantial Nb*/Al* disorder. Similar to SAN, the Al*$-$O distribution remains significantly broader than the Nb*$-$O distribution: $\sigma^2_{\text{Nb}*-\text{O}} \simeq 0.003$ Å^2 < $\sigma^2_{\text{Al}*-\text{O}} \simeq 0.008$ Å^2.

RMC refinements enable comprehensive statistical analyses of local distortions. Our previous studies (Krayzman *et al.*, 2008) using synthetic data for perovskite solid solutions indicated that simultaneous fitting of PDF and EXAFS enables recovery of high-order correlation functions that describe distortions of [BO_6] octahedra and, as such, are more infor-
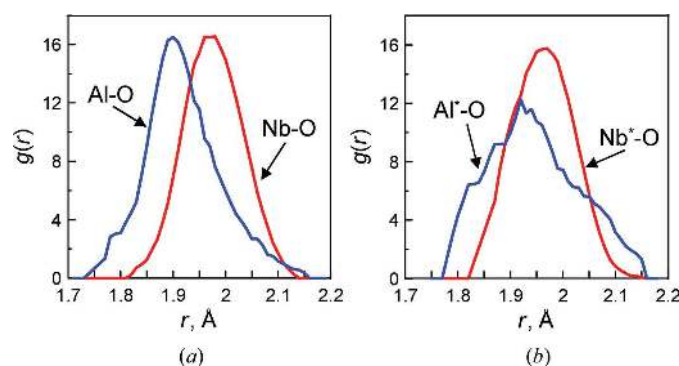

Figure 6
Partial Nb$-$O and Al$-$O PDFs obtained by RMC refinements for (a) SAN and (b) SANT.

mative than the partial PDFs. These high-order characteristics included statistical distributions of the average $B-O$ distances, $\langle R^{B-O} \rangle_i$, and their standard deviations, s_i^{B-O}, as calculated for each octahedron in the configuration:

$$\langle R^{B-O} \rangle_i = (1/6) \sum_{j=1}^{6} R_{ij}^{B-O},$$

$$s_i^{B-O} = \left\{ (1/6) \sum_{j=1}^{6} \left[R_{ij}^{B-O} - \langle R^{B-O} \rangle_i \right]^2 \right\}^{1/2}, \quad (9)$$

where R_{ij}^{B-O} represents the $B-O_j$ distances in the ith octahedron. Fig. 7 summarizes these distributions for the RMC-refined SAN and SANT configurations. The distributions of $\langle R^{B-O} \rangle_i$ exhibit similar widths for both SAN and SANT, despite their marked difference in the degree of LRO. However, the distributions of s_i^{B-O} for SANT are shifted toward larger values and are broader, with the most pronounced effect seen for the $[Al^*O_6]$ octahedra: that is, the structural strain due to the B-cation size mismatch in the partially disordered SANT is accommodated primarily by an increased distortion of the $[Al^*O_6]$ units. This result is consistent with weaker correlations identified for the $Al-O$ motion. Additional insight into octahedral distortion can be obtained by considering a correlation plot where each point relates the $\langle R^{B-O} \rangle_i$ and s_i^{B-O} values for the same octahedron (Fig. 8). A positive slope in these plots indicates a larger spread of the $B-O$ distances for the octahedra with larger values of $\langle R^{B-O} \rangle_i$. The $[NbO_6]$ octahedra in SAN display no significant 'size-distortion' correlation, whereas the $[Nb^*O_6]$ octahedra in SANT exhibit a weak positive trend. In contrast, the $[AlO_6]$ and $[Al^*O_6]$ octahedra in both SAN and SANT
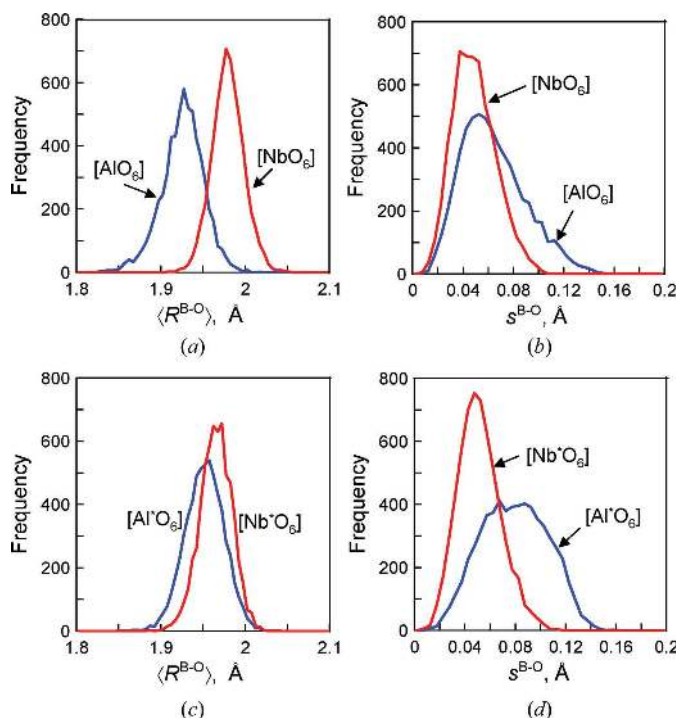
display a pronounced positive correlation. Overall, these results suggest that the $[AlO_6]$ octahedra are less rigid than the $[NbO_6]$ octahedra.

The anisotropy in the oxygen ADPs as observed for both SAN and SANT is common in perovskites and is often intuitively attributed to local octahedral tilting. Despite reproducing this anisotropy in the RMC refinements, we found no significant correlations among oxygen displacements that would mimic rigid unit rotations. In cubic SAN/SANT, phonons that involve octahedral rotations at room temperature likely exhibit relatively high frequencies because the tilting transition, if it exists, occurs well below room temperature. Therefore, such tilt-like displacements may be missing in the RMC-refined configurations because the total
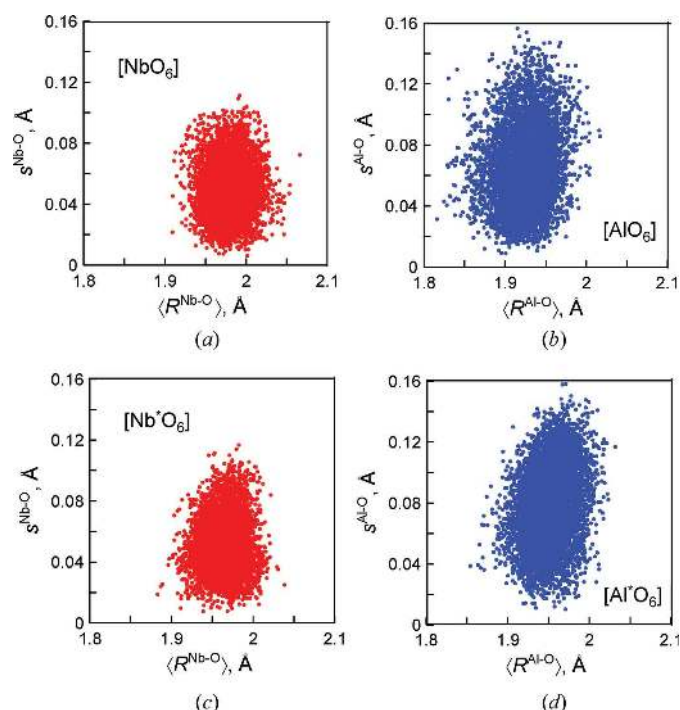

Figure 8
Correlation plots of s_i^{B-O} versus $\langle R^{B-O} \rangle_i$ for $[BO_6]$ octahedra in (a), (b) SAN and (c), (d) SANT.

Figure 7
Statistical distributions of (a), (c) $\langle R^{B-O} \rangle_i$ and (b), (d) s_i^{B-O} for $[BO_6]$ octahedra in (a), (b) SAN and (c), (d) SANT, respectively.
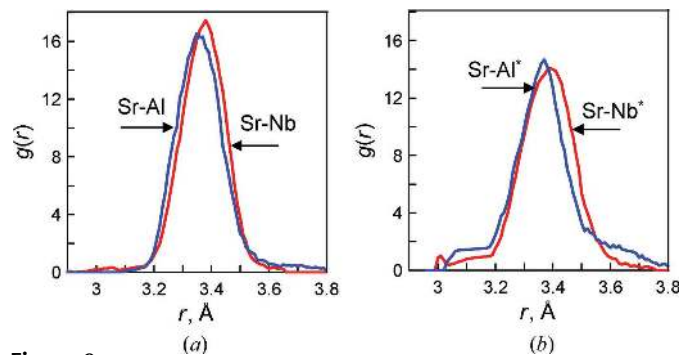

Figure 9
Partial PDFs Sr−Al and Sr−Nb obtained by RMC refinements for (a) SAN and (b) SANT. In SAN, Al and Nb are segregated into distinct sublattices. In contrast, in the partially disordered SANT, Al* and Nb* represent atomic sites that are distributed over Al-rich and Nb-rich sublattices.
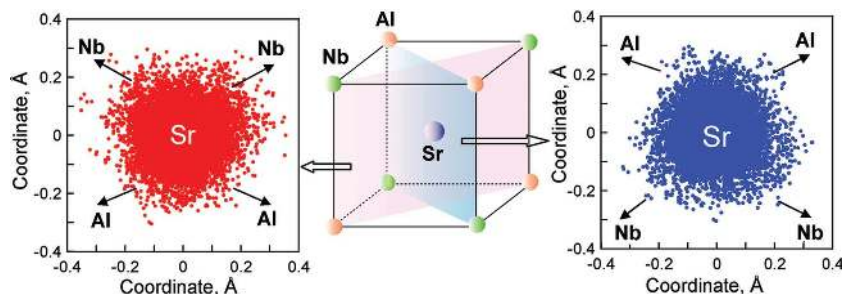
Figure 10
(Middle) Schematic drawing of the Sr coordination by Nb and Al in SAN. (Left, right) Projections of the Sr probability density function on the [110] and [1$\bar{1}$0] sections, respectively. Each point in these plots represents an instantaneous Sr position. Arrows indicate the directions toward the neighboring B cations. A pronounced complementary asymmetry of the two sections is observed.

scattering data have been shown to be primarily sensitive to low-frequency vibrational modes (Goodwin *et al.*, 2005).

Local displacements of Sr. In cubic double perovskites, the A sites exhibit T_d ($\bar{4}3m$) symmetry, which reflects a distribution of distinct B cations in the 1:1 ordered array (Fig. 2). In SAN, a peak maximum for the partial Sr—Al PDF (3.360 Å) occurs at a shorter distance than that for the Sr—Nb PDF (3.377 Å; Fig. 9a), yet the first statistical moments calculated for these Sr—Al/Sr—Nb distributions acquire very similar values of 3.373 Å (Sr—Al) and 3.374 Å (Sr—Nb). These first moments are slightly larger than the distance of 3.370 Å between the average Sr and Al/Nb positions, as expected, because of thermal disorder. The differences between the positions of the peak maxima and the first statistical moments are associated with the tails that appear on the long- and short-distance sides of the Sr—Al and Sr—Nb distributions, respectively. Similar effects are encountered in SANT (Fig. 9b).

We analyzed the effect of B-cation coordination on the local Sr displacements by reducing the refined RMC configuration into one unit cell and projecting the instantaneous Sr positions around a single crystallographic A site onto orthogonal (110) and (1$\bar{1}$0) sections (Fig. 10). In SAN, these two sections exhibit a striking complementary asymmetry. The probability density
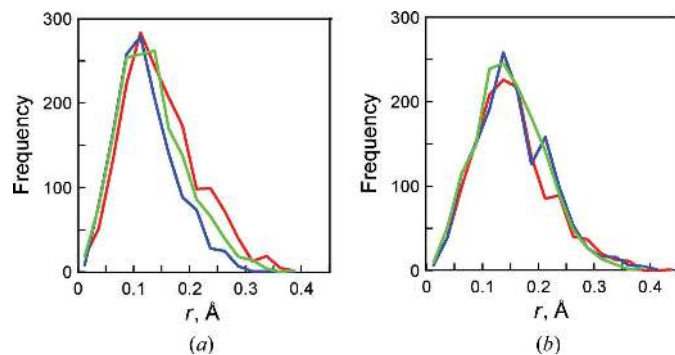
distribution for Sr appears to adopt the T_d symmetry of its crystallographic positions, with preferential Sr displacements toward the Nb cations. This result was reproducible regardless of the refinement path and the data-weighting scheme. In contrast to SAN, the Sr probability density distribution in SANT was isotropic, as expected for a strong Al*/Nb* disorder in this sample. Fig. 11 compares the probability distributions for the Sr atoms displaced within the cones directed toward Nb and Al, and the cones centered on the $\langle 100 \rangle_c$ directions. In SAN, the total number of Sr atoms per unit solid angle and the magnitude of their average displacements are the largest for the cones directed toward Nb, whereas the least preference is observed for the Al directions. In SANT, no such preferential displacement direction can be identified (Fig. 11b).

We estimated the energy difference between (1) the refined configuration, which featured an anisotropic probability density distribution for Sr, and (2) the configuration with all atoms except Sr held at their refined positions, while the Sr atoms were disordered according to a spherical Gaussian distribution. The differences in the Coulomb and short-range Sr—O interactions were considered. The A = 682.172 eV and ρ = 0.39450 Å parameters for the short-range Sr—O Born–Mayer potential, $Ae^{-r/\rho}$, were adopted from McCoy *et al.* (1997). Several ADP values (0.005, 0.007 and 0.010 Å^2) were tried for a Gaussian distribution of Sr.[2] The results revealed that an anisotropic distribution of Sr lowers the energy for both electrostatic (-0.06 eV) and short-range (-0.1 eV) interactions; the results were largely independent of the ADP value used to generate the Gaussian distribution. More accurate theoretical studies are warranted to verify this preliminary assessment.

Whether EXAFS data were critical to reveal the anisotropic Sr probability density function in SAN was tested by RMC refinements using just the total PDF and Bragg data. As expected, the agreement factors for these data sets improved slightly compared with the combined PDF/Bragg/EXAFS refinements. The major difference in the results obtained with and without EXAFS appeared in the first peaks of the Sr—B partial PDFs: The refinements without EXAFS data yielded similar positions of the peak maxima for both the Sr–Al and the Sr—Nb distributions. The resulting probability density function for Sr was isotropic. However, both the Nb and the Sr EXAFS data simulated for this configuration revealed large misfits with the experimental data for the Sr—B peaks. These results indicate that anisotropy in the Sr probability density distribution is supported by EXAFS data, which appear to be more sensitive to the separation of the peak maxima in the Sr—Nb and Sr—Al distributions than the total PDF.

Figure 11
Probability of Sr displacements toward the Nb sites (red), toward the Al sites (blue) and along the [100] directions (green) in (a) SAN and (b) SANT. In SAN, significant preference for the Sr displacements toward Nb is observed.

[2] Fitting an isotropic Gaussian to the refined Sr distribution yielded an ADP value of 0.007 Å^2.

V. Krayzman *et al.* · Combining total scattering and EXAFS data

research papers

5. Conclusions

RMC refinements that employ simultaneous fitting of the total scattering and EXAFS data were implemented as an extension to the public domain *RMCProfile* software and applied to metal Ni and perovskite-type $Sr(Al_{1/2}Nb_{1/2})O_3$ and its solid solution with $SrTiO_3$. The refinement algorithm takes into account both single- and multiple-scattering effects in EXAFS, thereby enabling accurate modeling of EXAFS data over several coordination shells around the absorber. Combining total scattering neutron PDF and Bragg data with element-specific Nb and Sr, EXAFS proved critical for recovering detailed, internally consistent local-structure characteristics that would not be obtained using the total scattering data alone because of a nearly complete overlap of the constituent partial PDFs. In particular, these combined refinements revealed T_d-like symmetry for the Sr probability density distribution in $Sr(Al_{1/2}Nb_{1/2})O_3$, which was overlooked by both conventional Rietveld refinements and RMC refinements using the neutron PDF/Bragg data. The anisotropic shape of the Sr distribution adopts the A-site point symmetry in cubic double perovskites and appears to lower the energies of both electrostatic and short-range interactions compared with a spherical shape. In addition to more accurate and detailed local-structure determination, simultaneous fitting of the total scattering and EXAFS data provides an effective means for benchmarking the EXAFS theory/approximations against total scattering PDF.

APPENDIX A
Calculation of EXAFS signal for double and triple scattering

The exact equation for a double-scattering (*i.e.* three-leg path, Fig. 12) contribution that involves an absorber i and scatterers j and n is expressed as

$$\chi_{ijn}^{(2)} = \mathrm{Im}\, C(\vartheta_{nij}) \frac{S_i^2 \Re F_j(\vartheta_{ijn}, k) F_n(\vartheta_{jni}, k)}{k r_{ij} r_{jn} r_{ni}}$$
$$\times \exp\left\{i[2kr_{\mathrm{eff}} + \psi_i(k)] - 2r_{\mathrm{eff}}/\lambda(k)\right\}. \qquad (10)$$

Here, $r_{\mathrm{eff}} = (r_{ij} + r_{jn} + r_{ni})/2$ is the effective scattering-path length, $F_j(\vartheta_{ijn}, k) = |F_j(\vartheta_{ijn}, k)| \exp[i\varphi_i(\vartheta_{ijn}, k)]$ is the complex scattering amplitude for an atom j and the scattering angle ϑ_{ijn}, and $C(\vartheta_{nij})$ is an angle-dependent parameter [in the plane-wave approximation $C(\vartheta_{nij}) = \cos\vartheta_{nij}$].
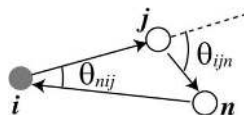
The *FEFF* code provides two real functions as an output:

Figure 12
A schematic representation of the double scattering in a three-leg path. The scattering process involves an absorber i and the scatterers j and n.

$$F^{\mathrm{effective}}(k) = \frac{\left|C(\vartheta_{nij}) F_j(\vartheta_{ijn}, k) F_n(\vartheta_{jni}, k)\right|}{r_{ij} r_{jn} r_{ni}} r_{\mathrm{eff}}^2, \qquad (11)$$
$$\varphi^{\mathrm{effective}}(k) = \arg C(\vartheta_{nij}) F_j(\vartheta_{ijn}, k) F_n(\vartheta_{jni}, k).$$

In the present RMC calculations, the contribution of double scattering to EXAFS is calculated using the approximate formula

$$\chi_{ijn}^{(2)} = \frac{S_i^2 \Re F_{jn}^{\mathrm{eff}(2)}(\vartheta, k)}{k r_{ij} r_{jn} r_{ni}} \sin\left[2kr_{\mathrm{eff}} + \psi_i(k) + \varphi_{jn}^{\mathrm{eff}(2)}(\vartheta, k)\right]$$
$$\times \exp\left[-2r_{\mathrm{eff}}/\lambda(k)\right], \qquad (12)$$

where the effective amplitude factor is

$$F_{jn}^{\mathrm{eff}(2)}(\vartheta, k) = \frac{\left|C(\vartheta_{nij}) F_j(\vartheta_{ijn}, k) F_n(\vartheta_{jni}, k)\right|}{r_{0\,\mathrm{eff}}^2} r_{0\,ij} r_{0\,jn} r_{0\,ni} \qquad (13)$$

and the effective phase correction is

$$\varphi_{jn}^{\mathrm{eff}(2)}(\vartheta, k) = \arg\left[C(\vartheta_{nij}) F_j(\vartheta_{ijn}, k) F_n(\vartheta_{jni}, k)\right]. \qquad (14)$$

Here r_{0ij} is the distance between the atoms i and j in the cluster used in *FEFF* calculations and $r_{0\mathrm{eff}} = (r_{0ij} + r_{0jn} + r_{0ni})/2$.

Similarly, contributions of the triple-scattering paths (Fig. 13) that involve either one or two scatterers are calculated according to the approximate formulae

$$\chi_{ijn}^{(3)} = \frac{S_i^2 \Re F_{jn}^{\mathrm{eff}(3)}(\vartheta_{ijn}, k)}{k r_{ij}^2 r_{jn}^2} \sin\left[2kr_{\mathrm{eff}} + \psi_i(k) + \varphi_{jn}^{\mathrm{eff}(3)}(\vartheta_{ijn}, k)\right]$$
$$\times \exp\left[-2r_{\mathrm{eff}}/\lambda(k)\right], \qquad (15a)$$

where $r_{\mathrm{eff}} = r_{ij} + r_{jn}$ (Fig. 13a),

$$\chi_{ij}^{(3)} = \frac{S_i^2 \Re F_j^{\mathrm{eff}(3)}(\pi, k)}{k r_{ij}^4} \sin\left[2kr_{\mathrm{eff}} + \psi_i(k) + \varphi_j^{\mathrm{eff}(3)}(\pi, k)\right]$$
$$\times \exp\left[-2r_{\mathrm{eff}}/\lambda(k)\right], \qquad (15b)$$

where $r_{\mathrm{eff}} = 2r_{ij}$ (Fig. 13b), and

$$\chi_{ijn}^{(3)} = \frac{S_i^2 \Re F_{jn}^{\mathrm{eff}(3)}(\vartheta_{nij}, k)}{k r_{ij}^2 r_{in}^2} \sin\left[2kr_{\mathrm{eff}} + \psi_i(k) + \varphi_{jn}^{\mathrm{eff}(3)}(\vartheta_{nij}, k)\right]$$
$$\times \exp\left[-2r_{\mathrm{eff}}/\lambda(k)\right], \qquad (15c)$$

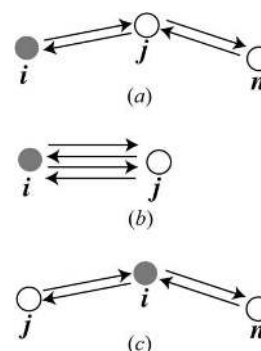where $r_{\mathrm{eff}} = r_{ij} + r_{in}$ (Fig. 13c).

Figure 13
Schematic representations of the triple scattering paths that involve two scatterers (*a*), (*c*) and a single scatterer (*b*). The absorber and scatterers are represented by filled and open circles, respectively.

Triple-scattering paths that involve three different scatterers are neglected in the present RMC refinements because of their small effect on the EXAFS signal.

APPENDIX B
EXAFS calculations for $SrAl_{0.4325}Nb_{0.4325}Ti_{0.135}O_3$

The EXAFS single-scattering contribution for the effective Al* atomic type was calculated as

$$
\begin{aligned}
\chi_i^{(\text{single})}(k) = & \frac{S_i^2 \Re_i(k) \exp[-2r/\lambda(k)]}{kr^2} \\
& \times \Big\{ 0.865 |F_{\text{Al}}(\pi, k)| \sin[2kr + \psi_i(k) + \varphi_{\text{Al}}(\pi, k)] \\
& + 0.135 |F_{\text{Ti}}(\pi, k)| \sin[2kr + \psi_i(k) + \varphi_{\text{Ti}}(\pi, k)] \Big\}. \quad (16)
\end{aligned}
$$

Rearranging equation (16), we obtain

$$
\begin{aligned}
\chi_i^{(\text{single})}(k) = & \frac{S_i^2 \Re_i(k) \exp[-2r/\lambda(k)]}{kr^2} \\
& \times |F_{\text{Al*}}(\pi, k)| \sin[2kr + \psi_i(k) + \varphi_{\text{Al*}}(\pi, k)], \quad (17)
\end{aligned}
$$

where the effective scattering amplitude and phases are

$$
\begin{aligned}
|F_{\text{Al*}}| = & \Big\{ |0.865 F_{\text{Al}}(\pi, k)|^2 + |0.135 F_{\text{Ti}}(\pi, k)|^2 \\
& + \big| 2 [0.865 F_{\text{Al}}(\pi, k) \, 0.135 F_{\text{Ti}}(\pi, k)] \big| \\
& \times \cos[\varphi_{\text{Al}}(\pi, k) - \varphi_{\text{Ti}}(\pi, k)] \Big\}^{1/2}, \quad (18)
\end{aligned}
$$

$$
\begin{aligned}
\varphi_{\text{Al*}}(\pi, k) = & \varphi_{\text{Al}}(\pi, k) + \arctan \Big(|0.135 F_{\text{Ti}}(\pi, k)| \\
& \times \sin[\varphi_{\text{Ti}}(\pi, k) - \varphi_{\text{Al}}(\pi, k)] / \{ |0.865 F_{\text{Al}}(\pi, k)| \\
& + |0.135 F_{\text{Ti}}(\pi, k)| \cos[\varphi_{\text{Ti}}(\pi, k) - \varphi_{\text{Al}}(\pi, k)] \} \Big). \quad (19)
\end{aligned}
$$

The single-scattering contribution for the effective Nb* site was calculated using similar equations. Analogous modifications were used to calculate multiple-scattering contributions.

References

Ankudinov, A. L., Bouldin, C., Rehr, J. J., Sims, J. & Hung, H. (2002). *Phys. Rev. B*, **65**, 104107.

Ankudinov, A. L., Ravel, B., Rehr, J. J. & Conradson, S. D. (1998). *Phys. Rev. B*, **58**, 7565–7576.

Billinge, S. J. L. & Levin, I. (2007). *Science*, **316**, 561–565.

Binsted, N., Stange, M., Owens, C., Fjellvåg, H. & Weller, M. T. (2001). *J. Synchrotron Rad.* **8**, 305–307.

Bozin, E. S., Schmidt, M., DeConinck, A. J., Paglia, G., Mitchell, J. F., Chatteriji, T., Radaelli, P. G., Proffen, Th. & Billinge, S. J. L. (2007). *Phys. Rev. Lett.* **98**, 137203.

Egami, T. & Billinge, S. J. L. (2003). *Underneath the Bragg Peaks, Structural Analysis of Complex Materials*. New York: Pergamon.

Farrow, C. L., Juhas, P., Liu, J. W., Bryndin, D., Bozin, E. S., Bloch, J., Proffen, Th. & Billinge, S. J. L. (2007). *J. Phys. Condens. Matter*, **19**, 335219.

Goodenough, J. B. & Longo, J. M. (1970). *Landolt Bornstein*, **4a**, 126–129.

Goodwin, A. L., Tucker, M. G., Cope, E. R., Dove, M. T. & Keen, D. A. (2005). *Phys. Rev. B*, **72**, 214304.

Guo, R., Bhalla, A. S., Sheen, J., Ainger, F. W., Erdei, S., Subbarao, E. C. & Cross, L. E. (1995). *J. Mater. Res.* **10**, 18–25.

Jeong, I.-K., Heffner, R. H., Graf, M. J. & Billinge, S. J. L. (2003). *Phys. Rev. B*, **67**, 104301.

Krayzman, V., Levin, I. & Tucker, M. G. (2008). *J. Appl. Cryst.* **41**, 705–714.

Masadeh, A. S., Bozin, E. S., Farrow, C. L., Paglia, G., Juhas, P., Billinge, S. J. L., Karkamkar, A. & Kanatzidis, M. G. (2007). *Phys. Rev. B*, **76**, 115413.

McCoy, M. A., Grimes, R. W. & Lee, W. E. (1997). *Philos. Mag. A*, **75**, 833–846.

McGreevy, R. L. (2001). *J. Phys. Condens. Matter*, **13**, R877–R913.

Mustre de Leon, J., Rehr, J. J., Zabinsky, S. I. & Albers, R. C. (1991). *Phys. Rev. B*, **44**, 4146–4156.

Peterson, P. F., Gutmann, M., Proffen, Th. & Billinge, S. J. L. (2000). *J. Appl. Cryst.* **33**, 1192.

Pradhan, S. K., Mao, Y., Wong, S. S., Chupas, P. & Petkov, V. (2007). *Chem. Mater.* **19**, 6180–6186.

Qiu, X., Proffen, Th., Mitchell, J. F. & Billinge, S. J. L. (2005). *Phys. Rev. Lett.* **94**, 177203.

Ravel, B. & Newville, M. (2005). *J. Synchrotron Rad.* **12**, 537–541.

Shannon, R. D. (1976). *Acta Cryst.* A**32**, 751–767.

Tucker, M. G., Keen, D. A., Dove, M. T., Goodwin, A. L. & Hui, Q. (2007). *J. Phys. Condens. Matter*, **19**, 335218.

Winterer, M., Delaplane, R. & McGreevy, R. (2002). *J. Appl. Cryst.* **35**, 434–442.